

The Boundary Conditions of the Heliosphere: Photoionization Models Constrained by Interstellar and *In Situ* Data

Jonathan D. Slavin¹ and Priscilla C. Frisch²

¹ Harvard-Smithsonian Center for Astrophysics, 60 Garden St., MS 83, Cambridge, MA 02138
e-mail: jslavin@cfa.harvard.edu

² University of Chicago, Department of Astronomy and Astrophysics, 5640 S. Ellis Ave., Chicago, IL 60637
e-mail: frisch@oddjob.uchicago.edu

Received – ; accepted –

ABSTRACT

Context. The boundary conditions of the heliosphere are set by the ionization, density and composition of inflowing interstellar matter.

Aims. Constraining the properties of the Local Interstellar Cloud (LIC) at the heliosphere requires radiative transfer ionization models.

Methods. We model the background interstellar radiation field using observed stellar FUV and EUV emission and the diffuse soft X-ray background. We also model the emission from the boundary between the LIC and the hot Local Bubble (LB) plasma, assuming that the cloud is evaporating because of thermal conduction. We create a grid of models covering a plausible range of LIC and LB properties, and use the modeled radiation field as input to radiative transfer/thermal equilibrium calculations using the Cloudy code. Data from *in situ* observations of He⁰, pickup ions and anomalous cosmic rays, and absorption line measurements towards ϵ CMA were used to constrain the input parameters.

Results. A restricted range of LIC H I column densities and LB plasma temperatures produce models that match all the observational data. The relative weakness of the constraints on $N(\text{H I})$ and T_h contrast with the narrow limits predicted for the H⁰ and electron density in the LIC at the Sun, $n(\text{H}^0) = 0.19 - 0.20 \text{ cm}^{-3}$, and $n_e = 0.07 \pm 0.01 \text{ cm}^{-3}$. Derived abundances are mostly typical for low density gas, with sub-solar Mg, Si and Fe, possibly subsolar O and N, and S about solar; however C is supersolar.

Conclusions. The ISM at the Sun is warm, low density, and partially ionized, with $n(\text{H}) \approx 0.23 - 0.27 \text{ cm}^{-3}$, $T \approx 6300 \text{ K}$, $\chi(\text{H}^+) \sim 0.2$, and $\chi(\text{He}^+) \sim 0.4$. These results appear to be robust since acceptable models are found for substantially different input radiation fields. Our results favor low values for the reference solar abundances for the LIC composition.

Key words. ISM: clouds — ISM: abundances — ultraviolet: ISM — X-rays: diffuse background – solar system: general — ISM: cosmic rays

1. Introduction

The solar wind evacuates a cavity in the interstellar medium (ISM) known as the heliosphere, from which interstellar ions are excluded. In contrast, neutral interstellar gas flows through the heliosphere until destroyed by charge-exchange with the solar wind and photoionization. These neutrals form the parent population of pickup ions (PUI) and anomalous cosmic rays (ACR) observed inside of the heliosphere. The properties of the surrounding interstellar medium set the boundary conditions of the heliosphere and determine its configuration and evolution. An ionization gradient is expected in the cloud feeding ISM into the heliosphere because of the hardness of the interstellar radiation field and the low opacity of the ISM (Cheng & Bruhweiler 1990; Vallerga 1996; Slavin & Frisch 2002, hereafter SF02). Because of this ionization gradient, the densities of partially ionized species in the LIC will differ from the values in the circum-heliosphere matter (CHM) that forms the boundary conditions of the heliosphere. Hence we have undertaken a series of studies to determine the boundary conditions of the heliosphere based on both astronomical and heliospheric data. In turn our results provide tighter constraints on the heliosphere models used to calculate the filtration factors for neutrals that allow comparisons between ISM inside and outside of the heliosphere.

The distribution and velocity of interstellar H⁰ inside of the heliosphere were first determined over 30 years ago from the fluorescence of solar Ly α radiation from these atoms (Thomas & Krassa 1971; Bertaux & Blamont 1971; Adams & Frisch 1977). Similar observations of solar 584Å fluorescence from interstellar He⁰ showed that H/He \sim 6 for interstellar gas inside of the heliosphere, in contrast to the cosmic value H/He=10 (Ajello 1978; Weller & Meier 1981). More recent measurements of $n(\text{H}^0)$ compared to $n(\text{He}^0)$ inside of the heliosphere find a similar ratio of H/He \sim 6–7 (Richardson et al. 2004; Gloeckler & Geiss 2004; Witte 2004; Möbius et al. 2004). This difference can be attributed to two effects: the loss of 40–60% of interstellar H⁰ due to charge-exchange with protons in the heliosheath region, a process denoted “filtration” (Ripken & Fahr 1983), and the hardness of the interstellar radiation field at the Sun that ionizes more He than H (§4).

The *Copernicus* satellite first showed that the local interstellar cloud (LIC) surrounding the Sun is low density, $\sim 0.1 \text{ atoms cm}^{-3}$, partially ionized ($n(\text{H}^+) \sim n(\text{H}^0)$, York 1974; McClintock et al. 1975), and warm (temperature $< 10^4 \text{ K}$, e.g. McClintock et al. 1978). *Copernicus*, FUSE and HST data have shown that the CLIC ISM has low column densities, $N(\text{H I}) < 10^{18.7}$, and N ionization levels of $> 30\%$, indicating similar H ionization because H and N ionizations are coupled by charge-exchange (Lehner et al. 2003; Wood et al. 2005). The low column densities of the LIC, $N(\text{H I}) < 10^{18} \text{ cm}^{-2}$, indicate it is par-

tially opaque to H ionizing radiation but not to He ionizing radiation. Cloud opacities of unity are reached for $N(\text{H I}) \sim 10^{17.2} \text{ cm}^{-2}$ for photons close to the ionization threshold of hydrogen (13.6 eV), and $N(\text{H I}) \sim 10^{17.7} \text{ cm}^{-2}$ for photons at the He^0 ionization edge (24.6 eV). The result is that the LIC is partially ionized with a significant ionization gradient between the edge and center. Because of this radiative transfer effects are important and need to be modeled carefully in order to determine the boundary conditions of the heliosphere.

The LIC belongs to a flow of low column density ISM embedded in the very low density and apparently hot ($T \sim 10^6 \text{ K}$) Local Bubble (Frisch 1981; Frisch & York 1986; McCammon et al. 1983; Snowden et al. 1990). The bulk motion of this cluster of local interstellar clouds (CLIC) through the local standard of rest¹ corresponds to a velocity of -19.4 km s^{-1} from the direction $\ell \sim 331^\circ$, $b \sim -5^\circ$. This upwind direction is towards the center of the Loop I superbubble and the center of the “ring” shadow that has been attributed to the merging of Loop I and the Local Bubble (Frisch & York 1986; Frisch 2007; Egger & Aschenbach 1995). Individual cloudlets with distinct velocities are identified in this flow (Lallement et al. 1986; Frisch et al. 2002). The cloud feeding interstellar gas into the heliosphere can be identified towards stars by the velocity of He^0 in the heliosphere measured by the GAS detector on Ulysses (Witte 2004). Curiously, ISM at the LIC velocity is not observed in the nearest gas in the upwind hemisphere, such as towards the closest star $\alpha \text{ Cen}$ or towards 36 Oph located beyond the heliosphere nose (Adams & Frisch 1977; Landsman et al. 1984; Linsky & Wood 1996; Wood et al. 2000a).

The lack of a velocity component at the LIC velocity towards either the nearest star $\alpha \text{ Cen}$, or towards 36 Oph, 5 pc away in the upwind direction (Wood et al. 2000b), indicates that the Sun is near the edge of the LIC, and that the CHM could vary over short timescales, even possibly over the few decades during which spacecraft observations have been carried out. The first interplanetary $\text{H}^0 \text{ Ly}\alpha$ spectrum obtained by *Copernicus* in 1975, when compared to $\text{Ly}\alpha$ spectra obtained during the mid-1990’s solar minimum conditions, indicates that the interstellar H^0 density in the inner heliosphere, where most of the backscattered $\text{Ly}\alpha$ emission occurs, has not varied due to cloud homogeneities, to within uncertainties (Frisch & Slavin 2005). This suggests the CHM density is relatively smooth over spatial scales of $\sim 120 \text{ AU}$ in the downwind direction (Frisch & Slavin 2005). It can now be shown that the CHM H^0 velocity also appears to have been constant over this period of time. The 1975 *Copernicus* data were acquired in the direction corresponding to ecliptic longitudes of $\lambda = 264.3^\circ$, $\beta = +15.0^\circ$, or $\sim 13.3^\circ$ from the most recent upwind direction derived from SOHO H I $\text{Ly}\alpha$ data (Qu  merais et al. 2006b,a, Q06). The *Copernicus* look direction was just outside of the “groove” expected in the $\text{Ly}\alpha$ glow in the ecliptic during solar minimum, which is caused by increased charge exchange in the solar wind current sheet, which has a small tilt during minimum conditions (Bzowski 2003). The velocity of the $\text{Ly}\alpha$ profile observed by *Copernicus* corresponds to $-24.8 \pm 2.6 \text{ km s}^{-1}$, after correction to the SOHO upwind direction. Since Q06 measured H^0 upwind velocities during the solar minimum years of 1996 and 1997 of $-25.7 \pm 0.2 \text{ km s}^{-1}$ and $-25.3 \pm 0.2 \text{ km s}^{-1}$, which is entirely consistent with the *Copernicus* results, we must arrive at the conclusion that the flow of interstellar H^0 into the heliosphere was relatively constant between the years of 1975 and 1997, so that any observations of

variations in the interplanetary $\text{Ly}\alpha$ glow properties must be due to solar activity properties alone. The thermal broadening of the *Copernicus* spectrum corresponded to a temperature of $\sim 5400 \text{ K}$, however measurement uncertainties allowed temperatures of up to 20,000 K.

In this paper we present new photoionization models of the LIC and show they reproduce both the densities of the ISM at the heliosphere and column densities in the LIC component towards the star $\epsilon \text{ CMA}$. In earlier papers, photoionization models of both the “LIC” and “Blue Cloud” components observed towards $\epsilon \text{ CMA}$ were used to constrain the models (SF02, Frisch & Slavin 2003). In the present paper only the LIC component towards $\epsilon \text{ CMA}$ and *in situ* observations of interstellar matter inside of the heliosphere are used to constrain the models.

The most truly unique quality of the LIC is that we are inside of it and therefore have the ability to sample the cloud directly via *in situ* observations carried out by a variety of spacecraft within the Solar System. Of all the available measurements of LIC gas flowing into the Solar System, the observations of the density and temperature of neutral He are apparently the most robust. Helium, unlike hydrogen, undergoes little ionization or heating in traversing the heliosheath regions, no deflection due to radiation pressure, and is destroyed by photoionization and electron-impact ionization within $\sim 1 \text{ AU}$ of the Sun, so we expect that the density and temperature of He^0 derived from the observations in the Solar System are truly representative of the values in the LIC (M  bius et al. 2004). In this paper we put a special emphasis on matching these He I data by determining model parameters that yield close agreement with the $n(\text{He}^0)$ and $T(\text{He}^0)$ data simultaneously.

2. Photoionization Model Constraints and Assumptions

The primary data constraints on our photoionization models are the LIC component column densities towards $\epsilon \text{ CMA}$, (Gry & Jenkins 2001, hereafter GJ01), *in situ* observations of He^0 (Witte 2004; M  bius et al. 2004), pickup ions (PUI, Gloeckler & Fisk 2007), and anomalous cosmic rays (ACR, Cummings et al. 2002). The astronomical and *in situ* observational constraints are summarized in Table 1.

2.1. Astronomical Constraints – The LIC towards $\epsilon \text{ CMA}$

The data toward $\epsilon \text{ CMA}$ of GJ01 show four separate velocity components detected in several different ions including C II, Si III, Si II, and Mg II. One of these velocity components, with a heliocentric velocity of $\sim 17 \text{ km s}^{-1}$,² is identified as the LIC. Another is identified with a second local cloud, the “Blue Cloud” (BC) at $\sim 10 \text{ km s}^{-1}$. In our previous study of LIC ionization (SF02) we noted that since the BC is close to the LIC, and both are detected towards Sirius at 2.7 pc (Lallement et al. 1994; H  brard et al. 1999), perhaps actually abutting the LIC, we should treat the two as a single cloud for this line of sight. Counter arguments to this line of reasoning include the fact that the BC apparently has different properties than the LIC, though whether it is colder or hotter is unclear (see H  brard et al. 1999, GJ01.). For this reason and because we wish to find the ionization models that best predict interstellar neutral densities inside and outside of the heliosphere, we assume in this paper that the

¹ Heliocentric motions are converted to the local standard of rest, LSR, using the Standard solar apex motion.

² Gry and Jenkins (2001) list the velocity of this component in the text as $16.2 \pm 1.5 \text{ km s}^{-1}$, compared to a projected LIC velocity of 15.1 km s^{-1} .

Table 1. Observational Constraints

Observed Quantity	Observed ^a Value	Notes ^b
$N(\text{C II})$ (cm^{-2})	$1.4 - 2.1 \times 10^{14}$	1
$N(\text{C II}^*)$ (cm^{-2})	$1.3 \pm 0.2 \times 10^{12}$	1, S
$N(\text{C IV})$ (cm^{-2})	$1.2 \pm 0.3 \times 10^{12}$	1
$N(\text{N I})$ (cm^{-2})	$1.70 \pm 0.05 \times 10^{13}$	1
$N(\text{O I})$ (cm^{-2})	$1.4^{+0.5}_{-0.2} \times 10^{14}$	1, S
$N(\text{Mg I})$ (cm^{-2})	$7 \pm 2 \times 10^9$	1
$N(\text{Mg II})$ (cm^{-2})	$3.1 \pm 0.1 \times 10^{12}$	1
$N(\text{Si II})$ (cm^{-2})	$4.52 \pm 0.2 \times 10^{12}$	1
$N(\text{Si III})$ (cm^{-2})	$2.3 \pm 0.2 \times 10^{12}$	1
$N(\text{S II})$ (cm^{-2})	$8.6 \pm 2.1 \times 10^{12}$	1
$N(\text{Fe II})$ (cm^{-2})	$1.35 \pm 0.05 \times 10^{12}$	1
$N(\text{H I})/N(\text{He I})$	14 ± 0.4^c	2
T (K)	6300 ± 340	4
$n(\text{He}^0)$ (cm^{-3})	0.015 ± 0.003	4, $f = 1^d$
$n(\text{N}^0)^e$ (cm^{-3})	$5.47 \pm 1.37 \times 10^{-6}$	3, $f = 0.76 - 1.07$
$n(\text{O}^0)^e$ (cm^{-3})	$4.82 \pm 0.53 \times 10^{-5}$	3, $f = 0.66 - 1.27$
$n(\text{Ne}^0)^e$ (cm^{-3})	$5.82 \pm 1.16 \times 10^{-6}$	3, $f = 0.88 - 0.95$
$n(\text{Ar}^0)^e$ (cm^{-3})	$1.63 \pm 0.73 \times 10^{-7}$	3, $f = 0.64 - 0.95$

^a $N(\text{C II}^*)$, $N(\text{N I})$, $N(\text{O I})$, $N(\text{Mg II})$, $N(\text{Si II})$, $N(\text{S II})$ and $N(\text{Fe II})$ are used to constrain the input abundances of the models.

^b The first number indicates the reference (below), and ‘‘S’’ indicates that the column density is based on a saturated line. Filtration factors (f , §2.2) are listed for neutrals that have been observed as pickup ions.

^c The uncertainty given is only that due to uncertainties listed in Dupuis et al. (1995) for the observed H I and He I column densities with the implicit assumption that the ratio is the same on all lines of sight. Given the substantial intrinsic variation in this ratio, however, the quoted uncertainty must be regarded as a lower limit to the true uncertainty.

^d We have assumed that $f = 1$ in this paper. The theoretical models yield $f = 0.94 - 1.10$ for He filtration.

^e Note that the pickup ion ratios are for values at the termination shock. N^0 , O^0 , Ne^0 , and Ar^0 densities need to be corrected for filtration in the heliosheath regions (2.2).

References: (1) Gry & Jenkins (2001) Note that the values shown are for the LIC component towards ϵ CMa.; (2) Dupuis et al. (1995); (3) Gloeckler & Fisk (2007); (4) Witte (2004).

LIC and BC are truly separate clouds and select only the LIC components towards ϵ CMa to constrain the models.

In the context of these models, the best astronomical constraints on the neutral ISM component are N I, the saturated O I line, and to some extent Mg I (though the line is weak). The electron density can be deduced from the ratio Mg II/Mg I, which is determined by photoionization and both dielectronic and radiative recombination; and the excitation of the C II fine-structure lines, C II/C II*. However, the heavy saturation of the C II 1335 Å line in the ISM limits the accuracy of the determination of $N(\text{C II})$, so in this paper we have de-emphasized C II/C II* as an ionization diagnostic. For a discussion of the use of C II/C II* and other observations in diagnosing the C abundance and C/S ratio see Slavin & Frisch (2006). Elements with first ionization potentials (FIP) < 13.6 eV (e.g. Mg, Si, S, and Fe) are generally almost entirely singly ionized in the LIC and thus the column densities of these ions are close to the total column densities for the elements.

2.2. In situ Constraints – He⁰, Pickup Ions, and Anomalous Cosmic Rays

Neutral atoms in the LIC penetrate the outer heliosphere regions, and become ionized primarily by charge transfer with the solar wind ions, photoionization, and electron impact ionization (Rucinski et al. 1996). The composition of this neutral population reflects the partially ionized state of the LIC, rather than indicating a pure FIP effect. Thus the abundances of high ionization potential elements such as He, Ne, and Ar, as well as H, do not reflect their elemental abundances directly. As a result, these neutrals provide an interesting and unique constraint on the photoionization models. Once ionized, these interstellar wind particles form a population of ions with a distinct velocity distribution that are ‘‘picked up’’ by the solar wind and convected outwards, where they are measured by various spacecraft (Möbius et al. 2004; Gloeckler & Geiss 2004). These pickup ions (PUI) are accelerated at the solar wind termination shock and form a population of cosmic rays with an anomalous composition reflective of their origin as interstellar neutrals in a partially ionized gas (Cummings et al. 2002). *In situ* observations of these byproducts of the ISM interaction with the heliosphere, H, He, N, O, Ar, and Ne, provide a unique opportunity to constrain theoretical models of an interstellar cloud using the combination of sightline-integrated data, and data from a ‘‘single’’ spatial location, the heliosphere.

We adopt the Ulysses He measurements as the best set of constraints on the ISM inside of the heliosphere. The Ulysses satellite provides direct measurements of interstellar He⁰ at high ecliptic latitudes throughout the solar cycle (the GAS detector, Witte 2004) and also measurements of the He pickup ion component (the SWICS detector Gloeckler & Geiss 2004; Gloeckler & Geiss 2007). Although interstellar He⁰ close to the Sun is detected through the resonant scattering of solar 584 Å radiation, geocoronal contamination of the interstellar signal is present so we prefer the Ulysses data (Möbius et al. 2004). We adopt the Ulysses GAS and SWICS results, $n(\text{He}^0) = 0.0151 \pm 0.0015 \text{ cm}^{-3}$, $T(\text{He}^0) = 6,300 \pm 340 \text{ K}$.

Data on the density of neutral N, O, Ne, and Ar in the surrounding ISM are provided by PUI and ACR data. The densities of interstellar N^0 , O^0 , Ne^0 , and Ar^0 at the termination shock are listed in Table 1. These densities must be corrected by the filtration factors, which correspond to the ratios of the densities at the termination shock to those in the LIC. Filtration occurs when neutral interstellar atoms are removed from the inflow by charge-exchange with interstellar protons as the atom crosses the heliosheath regions. The range of filtration values, f , calculated for the various elements are H: $f_{\text{H}} = 0.51 - 0.58$, He: $f_{\text{He}} = 0.94 - 1.10$, N: $f_{\text{N}} = 0.76 - 1.07$, O: $f_{\text{O}} = 0.66 - 1.27$, Ne: $f_{\text{Ne}} = 0.88 - 0.95$, and Ar: $f_{\text{Ar}} = 0.64 - 0.95$, depending on the underlying heliosphere model (Cummings et al. 2002; Müller & Zank 2004; Izmodenov et al. 2004). For He we adopt $f_{\text{He}} = 1$. The values of $f_{\text{O}} > 1$ indicate possible net creation of O^0 through charge transfer between O^+ and H^0 in the heliosheath regions. Our models must be compared to the interstellar densities obtained by correcting densities at the termination shock by filtration factors.

2.3. Interstellar Radiation Field at the Cloud Surface

The spectrum and flux of the cosmic radiation field control the ionization of the very local warm partially ionized medium (WPIM). The local interstellar radiation field (ISRF) that ionizes the LIC and other nearby cloudlets is determined by the location

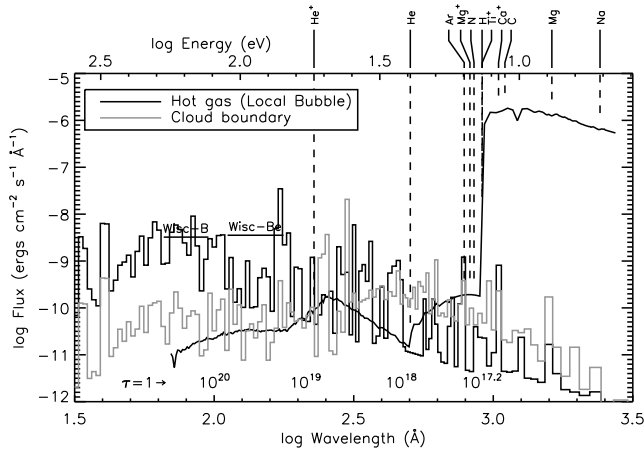


Fig. 1. The modeled interstellar radiation field at the Sun (model 26) is shown as a function of wavelength (bottom X-axis) and energy (top X-axis). The black histogram is the modeled hot gas (i.e. Local Bubble) spectrum while the gray histogram is the cloud boundary contribution. The other line is the stellar EUV/FUV background. The list of elements at the top of the plot identifies the ionization potentials for neutrals and ions of interest. The energy/wavelength at which an optical depth of 1 is reached for several different H I column densities is shown along the bottom of the plot. Observed flux levels of the soft X-ray diffuse background in the Wisconsin Be and B bands are plotted as lines (Bloch et al. 1986; McCammon et al. 1983).

of the Sun in the interior of a hole in the neutral interstellar gas and dust referred to as the Local Bubble. The clustering tendency of hot O and B stars, and attenuation of radiation by interstellar dust and gas, yield the well known spatial variation of the intensity and spectrum of the ISRF. We ignore possible temporal variations of the radiation field (e.g. Parravano et al. 2003), and model the ISRF throughout the LIC based on the observations of the present-day radiation field.

The radiation field we use in our models is based on observations of the ISRF at the Sun, supplemented by theoretical calculations of the spectra in the EUV and soft X-rays where lack of sensitivity and/or spectral resolution require the use of models to create a realistic spectrum. The directly observed radiation field includes the far ultraviolet (FUV) field created primarily by B stars, the extreme ultraviolet (EUV) field from two B stars (ϵ CMA and β CMA) and hot nearby white-dwarf stars, and the diffuse soft X-ray background (SXR). We show the radiation field at the cloud surface in Fig. 1. Because the interstellar opacity for radiation with $E > 13.6$ eV is vastly greater than for $E < 13.6$ eV, the EUV part of the ISRF originates in nearby regions with $N(\text{H I}) \lesssim 10^{18} \text{ cm}^{-2}$ while the FUV comes from a much larger volume.

We use the EUV field of Vallerga (1998), which is based on data collected by the Extreme Ultraviolet Explorer (EUVE) satellite. The EUVE spectrometers were sensitive over the wavelength range of 504 – 730 Å and showed that the stellar part of the EUV background is dominated by ϵ CMA and β CMA with substantial contributions from nearby hot white dwarfs at shorter wavelengths. Vallerga extrapolated those measurements to the H⁰ ionization edge at 912 Å using a total interstellar H⁰ density towards ϵ CMA of $N(\text{H I}) = 9 \times 10^{17} \text{ cm}^{-2}$. This value for $N(\text{H I})$ appears somewhat high based on observations of Gry & Jenkins (2001) which, though dependent on assumptions for gas phase

abundances, indicate a value for $N(\text{H I})$ of $\sim 7 \times 10^{17} \text{ cm}^{-2}$. This uncertainty in the total $N(\text{H I})$ affects only the extrapolated portion of the spectrum in our models since the other portion of the spectrum is derived by de-absorbing the observed spectrum by the value of $N(\text{H I})$ assumed just for the LIC. For the results presented here we have assumed that the total $N(\text{H I})$ towards ϵ CMA is $7 \times 10^{17} \text{ cm}^{-2}$. Assuming a larger value would increase the flux in the extrapolated region though our calculations indicate that the overall affect on our results is only at the $\sim 2\%$ level at most.

The FUV field is important because it sets the ionization rate of Mg⁰, which has a first ionization potential of 7.65 eV (1621 Å). The radiation field shortwards of 1600 Å is heavily dominated by O and B stars in Gould’s Belt, particularly those occupying the unattenuated regions of the third and fourth galactic quadrants. A pronounced spatial asymmetry in the 1565 Å radiation field has been observed by the TD-1 satellite S2/68 telescope survey of the interstellar radiation field, and we use those data and the extrapolation down to 912 Å from the 1564 Å measurements as calculated by Gondhalekar et al. (1980). The asymmetries in the TD-1 1565 Å radiation field are reproduced by diffuse interstellar radiation field models (Henry 2002).

The diffuse soft X-ray background has been observed over the entire sky at relatively low spatial and spectral resolution by *ROSAT* (Snowden et al. 1997) and proportional counters flown on sounding rockets by the Wisconsin group (e.g., McCammon et al. 1983). The broadband count rates in the low energy bands, particularly the B and C bands (130–188 eV and 160–284 eV respectively) have been modeled as coming from an optically thin, hot plasma at a temperature of $\sim 10^6$ K that occupies the low density cavity extending to ~ 50 –200 pc from the Sun in all directions (Snowden et al. 1990). Refinements to this picture have been required by *ROSAT* data showing absorption by relatively distant clouds (e.g. MBM12 Snowden et al. 1993). Snowden et al. (1998) propose a picture in which the emission is divided between a LB component (unabsorbed except for the LIC) and a distant absorbed component, mainly in the Galactic halo.

We model the spectrum measured by the broad-band soft X-ray observations by assuming that the SXR background consists of a local (unabsorbed) component and a distant (halo) component absorbed by an H I column density of 10^{19} cm^{-2} . The emission measure or intrinsic intensity of the local and distant components are assumed to be equal. The spectrum is calculated using the Raymond & Smith (1977, updated) plasma emission code assuming a hot, optically thin plasma in collisional ionization equilibrium. We explore temperatures for the hot gas of $\log T_h = 5.9, 6.0$ and 6.1 . The total flux, scaled by the emission measure, is fixed so that the B band flux matches the all-sky average from McCammon et al. (1983).

The boundary region between the warm LIC and the adjacent Local Bubble plasma may be another significant source of EUV radiation and we include this flux in our models 1–30. We model this transition region as a conductive interface between the LIC and Local Bubble plasma in the same way as described in (Slavin & Frisch 2002). The cloud is assumed to be steadily evaporating into the surrounding hot gas. The partially ionized gas of the LIC is heated and ionized as it flows into the Local Bubble. The ionization falls out of equilibrium, with low ionization stages persisting into the hot gas. The non-equilibrium ionization is followed and the emission in the boundary is calculated using an updated version of the Raymond & Smith (1977) code. Ions in the outflow are typically excited several times before being ionized and the boundary region radiates strongly in

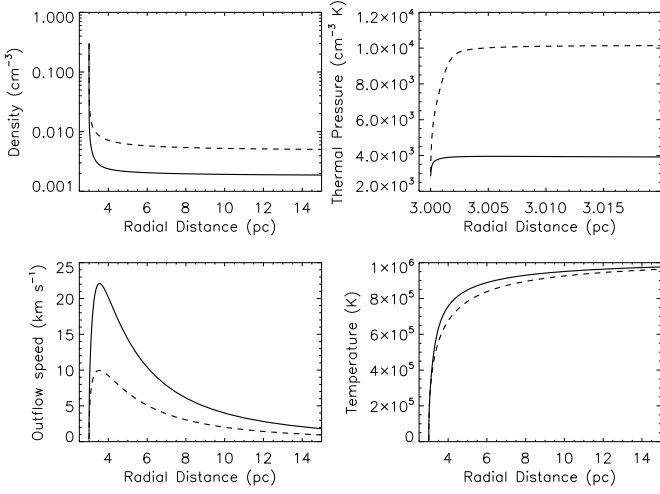


Fig. 2. Profiles of hydrodynamic variables in two different cloud boundary calculations. The solid lines are for model 6 which has $n_{\text{H}} = 0.273 \text{ cm}^{-3}$, $\log T_h = 6.0$, $B_0 = 2 \mu\text{G}$ and $N_{\text{HI}} = 4.5 \times 10^{17} \text{ cm}^{-2}$, while the dashed lines are for model 8, which differs from model 6 only in the strength of the magnetic field, $B_0 = 5 \mu\text{G}$. Note that in the upper right panel, the plot of thermal pressure, the radial scale is much smaller in order to show the variation in thermal pressure. The higher magnetic pressure inside the cloud for model 8 leads to the higher external thermal pressure for that case. The temperature profile differs in the two cases because the degree of heat flux saturation is reduced for the higher thermal pressure of model 8, which in turn leads to a shallower temperature gradient.

the 13.6 – 54.4 eV band. The contribution of the interface emission to the total B band flux is taken into account in the calculation of the emission measure for the hot gas of the Local Bubble so that the B band flux still matches the all-sky average.

An example of the profiles of the hydrodynamic variables for two different models is shown in Fig. 2. The magnetic field strength in these calculations is assumed to be proportional to the density at every point in the outflow. The treatment here is the same as in Slavin (1989) which contains a more thorough discussion of the issues involved in this sort of calculation. The effect of the field on the conductivity is parameterized in a simple way by a constant reduction factor of 0.5. The importance of the magnetic field for our calculations lies in the way it affects the thermal pressure in the layer. Since the density drops sharply in the outflow and $|B| \sim n$, any magnetic pressure ($\sim B^2$) drops even more sharply. The total pressure is roughly constant in the boundary, so the thermal pressure necessarily rises to make up for the decreasing magnetic pressure. Since all our models have nearly the same thermal pressure in the cloud, the primary effect of the magnetic field is to help determine the thermal pressure in the interface and thus radiative flux from the boundary. Since the total soft X-ray flux is fixed by requiring a match with the Wisconsin B band all-sky average count rate (McCammon et al. 1983), a larger assumed magnetic field increases only the EUV flux which is not constrained by the B-band data. The affect on the cloud of a larger EUV flux, as we discuss below, is to increase its temperature and ionization.

A secondary effect of the magnetic field can be seen in the temperature profiles in Figure 2. In evaporating clouds in the ISM, if the temperature gradient is large enough and the thermal pressure is low enough, the conduction becomes “saturated”,

Table 2. Model Input Parameter Values

Model No.	Input Parameter			
	n_{H} (cm^{-3})	$\log T_h$ (K)	B_0 (μG)	N_{HI} (10^{17} cm^{-2})
1	0.273	5.9	2.0	3.0
2	0.273	5.9	2.0	4.5
3	0.273	5.9	5.0	3.0
4	0.273	5.9	5.0	4.5
5	0.273	6.0	2.0	3.0
6	0.273	6.0	2.0	4.5
7	0.273	6.0	5.0	3.0
8	0.273	6.0	5.0	4.5
9	0.273	6.1	2.0	3.0
10	0.273	6.1	2.0	4.5
11	0.273	6.1	5.0	3.0
12	0.273	6.1	5.0	4.5
13	0.218	5.9	2.0	3.0
14	0.218	5.9	2.0	4.5
15	0.218	5.9	5.0	3.0
16	0.218	5.9	5.0	4.5
17	0.218	6.0	2.0	3.0
18	0.218	6.0	2.0	4.5
19	0.218	6.0	5.0	3.0
20	0.218	6.0	5.0	4.5
21	0.218	6.1	2.0	3.0
22	0.218	6.1	2.0	4.5
23	0.218	6.1	5.0	3.0
24	0.218	6.1	5.0	4.5
25	0.226	5.9	4.7	3.0
26	0.213	5.9	2.5	4.0
27	0.226	6.0	3.8	3.0
28	0.216	6.0	2.1	4.0
29	0.232	6.1	3.4	3.0
30	0.223	6.1	0.05	4.0
42	0.218	6.1	–	4.5

which means that the heat flux expected from the gas temperature and temperature gradient exceeds the flux that can be carried by the electrons (Cowie & McKee 1977). Saturation leads to a steepening of the temperature gradient and a relative slowing of the mass loss rate. In the two cases shown in Figure 2, the lower magnetic field case ($B_0 = 2 \mu\text{G}$) is moderately saturated (in terms of Cowie & McKee’s parameter, $\sigma_0 = 3$) while the other case ($B_0 = 5 \mu\text{G}$), because of the higher magnetic pressure, is less saturated.

3. Photoionization Models

The photoionization models of the LIC are developed following the same underlying procedure as in SF02, but selecting only the LIC absorption component towards $\epsilon \text{ CMa}$ for comparison. Improvements include using updated values for *in situ* ISM observations and using a recent version of the Cloudy radiative transfer/thermal equilibrium code (version 06.02.09a Ferland et al. 1998). We run Cloudy with the assumption of a plane-parallel cloud geometry and format our calculated photoionizing spectrum to be used as input. The selected options include utilizing recent calculations for the dielectronic recombination rates for $\text{Mg}^+ \rightarrow \text{Mg}^0$ (e.g. Altun et al. 2006, and the commands “set dielectronic recombination Badnell” and “set radiative recombination Badnell”), the assumption of constant pressure, and the inclusion of interstellar dust grains at 50% abundance compared to a standard ISM value. As we discuss below, the only role that dust plays is net heating of the gas since

there is far too little column for extinction to be important (expected $E(B - V) \sim 10^{-4.2}$). The fraction of the heating provided by dust is $\sim 4\%$ of the total heating, while dust provides $\sim 2\%$ of the cooling (mainly by capture of electrons onto grain surfaces). A cosmic ray ionization rate at the default background level of $2.5 \times 10^{17} \text{ s}^{-1}$ (for H ionization) is included. The LIC is assumed to be in ionization and thermal equilibrium, and Cloudy calculates the detailed transfer of radiation, including absorption and scattering of the radiation incident on the cloud surface, as well as the diffuse continuum and emission lines and continuum generated within the cloud.

The procedure for creating a model begins with generating the incident radiation field at the cloud surface (§2.3). The radiative transfer model is then run, and the output predictions of the model are compared to observations of interstellar absorption lines in the LIC towards $\epsilon \text{ CMa}$ ($N(\text{C II}^*)$, $N(\text{N I})$, $N(\text{O I})$, $N(\text{Mg II})$, $N(\text{S II})$, $N(\text{Si II})$, $N(\text{Fe II})$) and *in situ* observations of $n(\text{He}^0)$ by spacecraft inside of the solar system. The abundances of C, N, O, Mg, Si, S and Fe are then adjusted to be consistent with the observed column densities. With these new abundances, the Cloudy run is repeated and this process is continued until no adjustment of the abundances is needed. Because the abundances do have an impact on the emission from the cloud boundary, the cloud evaporation model is then re-run with the new abundances as well to re-generate the input ionizing spectrum. The iterative process of generating the spectrum and doing the Cloudy photoionization runs generally requires only a couple runs of the cloud evaporation program and a few runs of Cloudy.

4. Model Results

To investigate the dependence of the results on the input parameters we calculate a grid of 24 models. We explore total H density, $n_{\text{H}} = 0.273, 0.218$; Local Bubble hot gas temperature, $\log T_h = 5.9, 6.0, 6.1$; magnetic field strength, $B_0 = 2, 5 \mu\text{G}$; and H I column density, $N_{\text{HI}} = 3 \times 10^{17}, 4.5 \times 10^{17} \text{ cm}^{-2}$. The values for T and $n(\text{He}^0)$ at the solar location, the endpoint of the calculations, are shown in Fig. 3 for this set of models. We then explore another six models in which we do the calculations over a grid in $\log T_h$ and N_{HI} but vary the values of n_{H} and B_0 in order to match the observed T and $n(\text{He}^0)$. We employed a multiple linear regression to assist in narrowing down the search region for the values of n_{H} and B_0 needed to match the observations. Since the dependencies of the results on the parameters really are quite non-linear, this procedure could not work to predict exactly correct values for the required parameters, but was useful for getting close to the correct values. Based on the results for the initial grid of models, we use $\log T_h = 5.9, 6.0, 6.1$ and $N_{\text{HI}} = 3 \times 10^{17}, 4 \times 10^{17} \text{ cm}^{-2}$ for this smaller grid, models 25–30. We chose to use $4 \times 10^{17} \text{ cm}^{-2}$ rather than $4.5 \times 10^{17} \text{ cm}^{-2}$ because the higher column density models, for the most part, produced temperatures that were too high. As can be seen from Fig. 3, all of these models (25–30), plotted as stars, are consistent with the observed T and $n(\text{He}^0)$, indicated by the ellipse in the figure. Table 2 gives the input parameters for each model. Model predictions for the $\epsilon \text{ CMa}$ sightline integrated through the LIC are presented in Table 3. Model predictions for the CHM (i.e. at the solar location) are shown in Table 4.

In SF02 we tested models with no emission from the cloud boundary. This amounts to assuming that the boundary is a sharp transition from the hot gas of the Local Bubble to the warm gas of the LIC. We have again explored such models using the LIC data as constraints in the same way as for the models discussed above with a conductive interface. When there is no evaporative

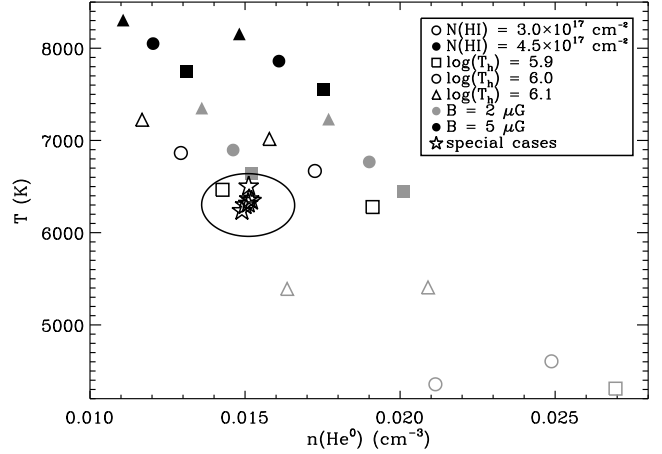


Fig. 3. Model results for the He^0 density and temperature in the ISM just outside the heliosphere. The squares, circles, and triangles are for models that are part of the initial grid of 24 models, while the stars are for models 25 – 30 for which the magnetic field, B , and the total H density, n_{H} , were varied to match the observed $n(\text{He}^0)$ and T . For the grid models, the empty symbols are for models with $N(\text{H I}) = 3 \times 10^{17} \text{ cm}^{-2}$, while the filled symbol models have $N(\text{H I}) = 4.5 \times 10^{17} \text{ cm}^{-2}$. As the legend shows, the color (black vs. gray) indicates the magnetic field strength and the symbol shape indicates the temperature assumed for the hot gas of the Local Bubble. For identical kinds of points, the one to the left is for a model with $n(\text{H}^0) = 0.218 \text{ cm}^{-3}$ and the one to the right has $n(\text{H}^0) = 0.273 \text{ cm}^{-3}$. The ellipse is the error range around the observed values for $n(\text{He}^0)$ and T .

boundary, our models do not depend on the magnetic field in the cloud since in that case the ionizing flux consists only of diffuse emission from the hot gas of the Local Bubble and EUV emission from nearby hot stars and the spectrum is not related to the properties of the cloud. For these models our model grid consists of total H density, $n_{\text{H}} = 0.273, 0.218$, Local Bubble hot gas temperature, $\log T_h = 5.9, 6.0, 6.1$, and H I column density, $N_{\text{HI}} = 3 \times 10^{17}, 4.5 \times 10^{17} \text{ cm}^{-2}$, for a total of twelve models that we label as models 31–42. Of these models, however, only two resulted in ionizing fluxes sufficient to heat the cloud to a temperature $\sim 6000 \text{ K}$ at the same time as matching the constraints on the ion column densities. These models were the ones with $\log T_h = 6.1$ and $N_{\text{HI}} = 4.5 \times 10^{17} \text{ cm}^{-2}$ (models 36 and 42). For the other cases, either at the surface or deeper into the cloud, there are insufficient photons to provide the heating to balance the cooling and the cloud temperature drops sharply to $< 1000 \text{ K}$. The model with $n_{\text{H}} = 0.218$ (model 42) is consistent with the observed value of $n(\text{He}^0)$ and with the column density data as well.³

From these 42 models we have selected those that provide acceptable results for the observational constraints, according to prioritized requirements. The first requirement is that the model predict the density and temperature of He I observed inside of the solar system. Models 14 (marginally), 15 and 25–30 and 42 predict a He density and temperature consistent with the observed values within the reported errors. They also predict the PUI Ne densities, for an assumed Ne/H=123 ppm. Models 26 and 28 successfully match the PUI data for Ne/H as low as

³ Whether or not model 42 is the answer to the meaning of life, the universe and everything remains to be seen.

Table 3. Model Column Density Results

Model	$\log N(\text{H}_{\text{tot}})$	$\log N(\text{Ar I})$	$\log N(\text{Ar II})$	$\log N(\text{Si III})$	$\frac{N(\text{Mg II})}{N(\text{Mg I})}$	$\frac{N(\text{C II})}{N(\text{C II}^*)}$	$\frac{N(\text{H I})}{N(\text{He I})}$
Obs. ^a				12.40	443^{+197}_{-110}	93 – 430 ^b	12 – 16
1	17.58	11.48	11.76	8.895	706.3	213.0	11.36
2	17.78	11.67	11.95	9.641	325.3	234.1	11.40
3	17.65	11.33	11.84	9.844	246.1	182.1	11.44
4	17.82	11.55	12.00	10.12	136.5	198.0	11.80
5	17.58	11.49	11.75	8.961	717.8	230.0	11.62
6	17.78	11.67	11.94	9.711	286.7	244.9	11.62
7	17.64	11.34	11.81	9.909	207.4	194.8	12.47
8	17.82	11.56	11.97	10.17	119.7	208.2	12.66
9	17.59	11.46	11.75	9.289	553.0	239.5	12.27
10	17.78	11.66	11.93	9.861	210.3	248.1	12.14
11	17.64	11.33	11.78	9.993	171.2	201.7	13.44
12	17.82	11.54	11.95	10.23	104.3	210.6	13.52
13	17.60	11.44	11.78	9.100	768.9	255.1	11.52
14	17.79	11.64	11.96	9.738	336.4	274.4	11.47
15	17.67	11.30	11.85	9.944	251.2	215.9	11.65
16	17.84	11.51	12.01	10.21	140.6	232.1	12.01
17	17.58	11.47	11.76	8.926	840.1	262.5	11.65
18	17.79	11.65	11.95	9.792	308.9	286.3	11.64
19	17.66	11.30	11.82	10.02	208.5	229.2	12.76
20	17.84	11.52	11.98	10.26	123.5	242.1	12.95
21	17.59	11.43	11.76	9.318	633.1	280.8	12.41
22	17.79	11.63	11.94	9.926	224.9	288.4	12.25
23	17.66	11.29	11.79	10.10	175.0	235.5	13.81
24	17.84	11.50	11.96	10.31	110.2	245.5	13.85
25	17.66	11.32	11.84	9.887	271.3	213.6	11.71
26	17.74	11.56	11.91	9.676	383.9	270.1	11.70
27	17.63	11.36	11.79	9.751	331.1	242.0	12.51
28	17.73	11.59	11.90	9.625	411.6	284.5	11.79
29	17.62	11.38	11.77	9.720	329.3	251.6	13.01
30	17.72	11.60	11.88	9.642	386.6	295.1	12.08
42	17.77	11.70	11.92	9.555	482.9	317.9	11.51

^a Observational results from Gry & Jenkins (2001) (see table 1). The values listed for $N(\text{H I})/N(\text{He I})$ are the range of values observed excluding Feige 24 which is one of the most distant stars observed by Dupuis et al. (1995) and has unusually large $N(\text{H I})$ and ratio values.

^b The upper limit on $N(\text{C II})$ is not well determined observationally because of the saturation of the line. Gry & Jenkins (2001) define it by assuming a solar C/S abundance ratio and using the observed S II column density. We find (see Slavin & Frisch 2006) that the abundance of C required to match the $N(\text{C II}^*)$ observations is supersolar, with C/S ~ 36 – 44, which results in a much higher upper limit on $N(\text{C II})$.

~ 100 ppm. These models are also required to match the observed Mg II/Mg I ratio in the LIC towards ϵ CMa. Models 14, 27, and 29 marginally fit this criterion, while 26, 28, 30, and 42 successfully fit this criterion. Note that the new models now provide acceptable predictions for the CHM temperature, which was not the case for the best models in SF02. These models are also consistent with the observed C II/C II* ratios in the LIC component towards ϵ CMa though this constraint is weak because of the large uncertainties in $N(\text{C II})$. Based on these comparisons, and given the uncertainties in both data and models, Models 14, 26-30, and 42 are plausible models, but Models 26 and 28 appear to best match the observational constraints.

Based on the constraints and assumptions presented in the previous section, we select models 14, 26–30 and 42 as the best models for the LIC ionization, with models 26 and 28 favored by the PUI Ne data provided that Ne/H > 100 ppm. We believe that these seven models then give a realistic range for the uncertainties in the boundary conditions of the heliosphere, providing that the underlying assumptions implicit in the Cloudy code, e.g. photoionization equilibrium, are correct. The predictions of the best models provide excellent matches to the observational constraints. Based on these models, we find the boundary conditions of the heliosphere to be describable as $n(\text{H}^0) = 0.19 - 0.20 \text{ cm}^{-3}$,

$n_e = 0.05 - 0.08 \text{ cm}^{-3}$, and $\chi(\text{H}) \equiv \text{H}^+ / (\text{H}^0 + \text{H}^+) = 0.19 - 0.26$, $\chi(\text{He}) \equiv \text{He}^+ / (\text{He}^0 + \text{He}^+) = 0.36 - 0.43$. For these models, we find abundances of O/H = 295 – 437 ppm, C/H = 589 – 813 ppm, and N/H = 40.7 – 64.6 ppm (Table 7). The total LIC density is $n(\text{H})_0 = 0.213 - 0.232 \text{ cm}^{-3}$, while the strength of the interstellar magnetic in the cloud varies between 0 and 3.8 μG . The Ne PUI data further favor densities of $n(\text{H}^0) \approx 0.19 \text{ cm}^{-3}$ and $n_e = 0.06 - 0.07 \text{ cm}^{-3}$.

The radiation field incident on the LIC for Model 26 is shown in Fig. 1 and the spectral characteristics of the field for each model are listed in Table 5. The wavelengths regions $\lambda \leq 912 \text{ \AA}$ and $\lambda \sim 1500 \text{ \AA}$ are of primary importance for the photoionization of the cloud, the former because it determines H^0 and He^0 ionization, and the latter because it determines Mg^0 ionization.

The ionization parameter is defined as $U \equiv \Phi/n(\text{H})c$, where Φ is the H ionizing photon flux, $n(\text{H})$ is the total (neutral + ionized) hydrogen density at the cloud surface and c is the speed of light. The total ionizing photon fluxes at the cloud surface (photons $\text{cm}^{-2} \text{ s}^{-1}$) for the three bands 13.6–24.6, 24.6–54.4, and 54.4–100 eV, are given by Φ_{H} , Φ_{He^0} , and Φ_{He^+} , respectively. The ratio of the total number of H^0 and He^0 ionizing photons in the incident radiation field is given by $Q(\text{He}^0)/Q(\text{H}^0)$. The quantity $\langle E \rangle$ (eV) is the mean energy of an ionizing photon, equal to the

Table 4. Model Results for Solar Location

Model	X(H)	X(He)	$n(\text{H I})$	$n(\text{He I})$	$n(\text{N I})$	$n(\text{O I})$	$n(\text{Ne I})$	$n(\text{Ar I})$	n_e	n_p	T
Obs. ^a				0.015	5.5×10^{-6}	4.8×10^{-5}	5.8×10^{-6}	1.6×10^{-7}			6300
1	0.176	0.299	0.318	0.0269	1.84×10^{-5}	1.48×10^{-4}	1.39×10^{-5}	3.47×10^{-7}	0.0800	0.0678	4310
2	0.196	0.352	0.251	0.0201	9.63×10^{-6}	7.71×10^{-5}	8.51×10^{-6}	2.69×10^{-7}	0.0724	0.0611	6450
3	0.286	0.404	0.230	0.0191	1.34×10^{-5}	1.07×10^{-4}	7.81×10^{-6}	1.82×10^{-7}	0.106	0.0922	6280
4	0.259	0.428	0.229	0.0175	8.86×10^{-6}	6.95×10^{-5}	6.45×10^{-6}	1.92×10^{-7}	0.0937	0.0799	7560
5	0.174	0.310	0.300	0.0249	1.72×10^{-5}	1.39×10^{-4}	1.13×10^{-5}	3.30×10^{-7}	0.0750	0.0631	4610
6	0.197	0.363	0.242	0.0190	9.13×10^{-6}	7.44×10^{-5}	7.08×10^{-6}	2.61×10^{-7}	0.0707	0.0593	6770
7	0.278	0.441	0.225	0.0173	1.33×10^{-5}	1.04×10^{-4}	5.75×10^{-6}	1.78×10^{-7}	0.101	0.0866	6670
8	0.257	0.459	0.223	0.0161	8.65×10^{-6}	6.79×10^{-5}	4.92×10^{-6}	1.89×10^{-7}	0.0918	0.0773	7860
9	0.193	0.357	0.265	0.0209	1.53×10^{-5}	1.23×10^{-4}	7.52×10^{-6}	2.71×10^{-7}	0.0761	0.0634	5410
10	0.203	0.392	0.235	0.0177	9.06×10^{-6}	7.24×10^{-5}	5.52×10^{-6}	2.43×10^{-7}	0.0723	0.0600	7230
11	0.278	0.474	0.220	0.0158	1.29×10^{-5}	1.02×10^{-4}	4.42×10^{-6}	1.69×10^{-7}	0.0999	0.0847	7020
12	0.262	0.490	0.219	0.0148	8.41×10^{-6}	6.66×10^{-5}	3.83×10^{-6}	1.78×10^{-7}	0.0928	0.0776	8160
13	0.201	0.333	0.230	0.0191	1.34×10^{-5}	1.08×10^{-4}	8.94×10^{-6}	2.32×10^{-7}	0.0681	0.0580	4720
14	0.215	0.376	0.193	0.0152	7.29×10^{-6}	5.95×10^{-5}	5.99×10^{-6}	1.94×10^{-7}	0.0625	0.0528	6650
15	0.310	0.436	0.176	0.0143	1.02×10^{-5}	8.18×10^{-5}	5.35×10^{-6}	1.28×10^{-7}	0.0905	0.0789	6470
16	0.284	0.461	0.175	0.0131	6.76×10^{-6}	5.36×10^{-5}	4.40×10^{-6}	1.35×10^{-7}	0.0812	0.0695	7750
17	0.178	0.315	0.255	0.0211	1.47×10^{-5}	1.19×10^{-4}	9.51×10^{-6}	2.75×10^{-7}	0.0656	0.0553	4360
18	0.214	0.383	0.188	0.0146	7.16×10^{-6}	5.81×10^{-5}	5.07×10^{-6}	1.91×10^{-7}	0.0610	0.0513	6900
19	0.302	0.472	0.173	0.0129	1.01×10^{-5}	8.03×10^{-5}	3.93×10^{-6}	1.26×10^{-7}	0.0872	0.0748	6860
20	0.282	0.491	0.172	0.0120	6.61×10^{-6}	5.26×10^{-5}	3.37×10^{-6}	1.33×10^{-7}	0.0802	0.0677	8050
21	0.204	0.374	0.211	0.0164	1.20×10^{-5}	9.85×10^{-5}	5.54×10^{-6}	2.04×10^{-7}	0.0648	0.0541	5390
22	0.221	0.414	0.184	0.0136	6.96×10^{-6}	5.69×10^{-5}	3.90×10^{-6}	1.78×10^{-7}	0.0628	0.0523	7350
23	0.305	0.506	0.168	0.0117	9.91×10^{-6}	7.82×10^{-5}	2.97×10^{-6}	1.18×10^{-7}	0.0868	0.0737	7220
24	0.286	0.520	0.169	0.0111	6.57×10^{-6}	5.16×10^{-5}	2.60×10^{-6}	1.25×10^{-7}	0.0808	0.0676	8310
25	0.297	0.427	0.187	0.0151	1.09×10^{-5}	8.67×10^{-5}	5.75×10^{-6}	1.41×10^{-7}	0.0907	0.0789	6360
26	0.224	0.385	0.192	0.0151	8.32×10^{-6}	6.66×10^{-5}	5.96×10^{-6}	1.83×10^{-7}	0.0653	0.0554	6320
27	0.258	0.426	0.195	0.0149	1.13×10^{-5}	8.97×10^{-5}	5.03×10^{-6}	1.63×10^{-7}	0.0796	0.0677	6240
28	0.212	0.376	0.194	0.0152	8.24×10^{-6}	6.73×10^{-5}	5.49×10^{-6}	1.95×10^{-7}	0.0622	0.0523	6350
29	0.242	0.429	0.202	0.0150	1.17×10^{-5}	9.30×10^{-5}	4.53×10^{-6}	1.74×10^{-7}	0.0769	0.0646	6300
30	0.203	0.379	0.197	0.0151	8.51×10^{-6}	6.81×10^{-5}	4.78×10^{-6}	2.01×10^{-7}	0.0605	0.0502	6500
42	0.189	0.355	0.186	0.0145	6.91×10^{-6}	5.71×10^{-5}	4.60×10^{-6}	2.04×10^{-7}	0.0522	0.0433	6590

^a Observational results from Gloeckler & Geiss (2004), Gloeckler (2005, private communication) and Witte et al. (1996) (see table 1 for uncertainties).

integrated energy flux from 13.6 to 100 eV divided by the integrated photon flux over the same energy range.

In Figure 3 we show $n(\text{He}^0)$ and temperature of the CHM for our model calculations. In Figure 4 we show $N_{\text{H}}/N_{\text{I}}$ vs. $\text{Mg II}/\text{Mg I}$, illustrating that $\text{Mg II}/\text{Mg I}$ is sensitive to both ionized and neutral material. The ionization of the CHM is listed in Table 6 for Model 26, where commonly observed elements are listed. The abundances of He, Ne, Na, Al, P, Ar, and Ca were assumed, based on solar abundances, and were not adjusted in the modeling process. The abundances of C, N, O, Mg, Si, S and Fe were adjusted for each model to match observed column densities towards ϵ CMa (see §2). The elemental abundances that have been assumed, with the exception of that for He, are not expected to have any significant impact on the model results.

5. Discussion

5.1. Heliosphere Boundary Conditions

As discussed above, the best models of those we calculated are determined by the match to the CHM He^0 density and temperature found by the *in situ* Ulysses measurements (§2.2), combined with the matching the LIC component column density ratios $\text{Mg II}/\text{Mg I}$ and $\text{C II}/\text{C I}^*$. These models span a fairly large range in the model parameters: $n_{\text{H}} = 0.213 - 0.232 \text{ cm}^{-3}$, $\log T_h = 5.9 - 6.1 \text{ K}$, $B_0 = 0.05 - 3.8 \mu\text{G}$, and $N(\text{H I}) = 3.0 \times 10^{17} - 4.5 \times 10^{17}$

Table 6. Model 26 Results for Ionization Fractions^a

Element	PPM	I	II	III	IV
H	10^6	0.776	0.224	–	–
He	10^5	0.611	0.385	4.36(-3)	–
C	661	2.68(-4)	0.975	0.0244	0.000
N	46.8	0.720	0.280	8.52(-5)	0.000
O	331	0.814	0.186	4.71(-5)	0.000
Ne	123	0.196	0.652	0.152	2.79(-6)
Na	2.04	1.47(-3)	0.843	0.155	6.34(-6)
Mg	6.61	1.98(-3)	0.850	0.148	0.000
Al	0.0794	5.37(-5)	0.976	0.0118	0.0123
Si	8.13	4.21(-5)	0.999	8.02(-4)	3.10(-5)
P	0.219	1.35(-4)	0.977	0.0232	9.29(-5)
S	15.8	6.47(-5)	0.971	0.0288	1.95(-6)
Ar	2.82	0.263	0.500	0.238	2.83(-6)
Ca	4.07(-4)	9.21(-6)	0.0155	0.984	1.87(-4)
Fe	2.51	7.01(-5)	0.975	0.0245	5.75(-6)

^a Numbers less than 10^{-3} are written as x(y) where y is the exponent and x is the mantissa (or significant).

cm^{-2} . Despite this, the predicted values for neutral H density and electron density in the CHM lie within a remarkably small range: $n(\text{H}^0) = 0.19 - 0.20 \text{ cm}^{-3}$, $n_e = 0.05 - 0.08 \text{ cm}^{-3}$, for models that include the conductive boundary. For the one model with-

Table 5. Characteristics of the Model Radiation Field

Model	U	ϕ_{H} photons $\text{cm}^{-2} \text{s}^{-1}$	ϕ_{He^0} photons $\text{cm}^{-2} \text{s}^{-1}$	ϕ_{He^+} photons $\text{cm}^{-2} \text{s}^{-1}$	$Q(\text{He}^0)/Q(\text{H}^0)$	$\langle E \rangle$ eV
1	2.0×10^{-6}	4.6×10^3	7.5×10^3	2.8×10^3	0.46	74.6
2	2.0×10^{-6}	5.3×10^3	7.3×10^3	2.7×10^3	0.44	72.4
3	3.1×10^{-6}	9.0×10^3	1.3×10^4	2.7×10^3	0.49	57.7
4	3.0×10^{-6}	8.6×10^3	1.2×10^4	2.6×10^3	0.49	58.6
5	2.0×10^{-6}	4.0×10^3	7.0×10^3	3.8×10^3	0.43	79.0
6	2.1×10^{-6}	4.9×10^3	6.9×10^3	3.8×10^3	0.41	76.2
7	3.2×10^{-6}	7.4×10^3	1.4×10^4	3.8×10^3	0.53	61.3
8	3.1×10^{-6}	7.4×10^3	1.3×10^4	3.7×10^3	0.52	61.5
9	2.2×10^{-6}	3.8×10^3	7.4×10^3	5.6×10^3	0.40	80.0
10	2.3×10^{-6}	4.8×10^3	7.2×10^3	5.6×10^3	0.38	77.3
11	3.5×10^{-6}	6.6×10^3	1.5×10^4	5.6×10^3	0.53	63.4
12	3.4×10^{-6}	6.9×10^3	1.5×10^4	5.5×10^3	0.52	63.2
13	2.3×10^{-6}	4.3×10^3	7.0×10^3	2.8×10^3	0.46	76.9
14	2.4×10^{-6}	5.1×10^3	6.8×10^3	2.7×10^3	0.43	74.3
15	3.7×10^{-6}	8.5×10^3	1.2×10^4	2.7×10^3	0.49	58.8
16	3.6×10^{-6}	8.2×10^3	1.2×10^4	2.6×10^3	0.49	59.5
17	2.3×10^{-6}	3.7×10^3	6.4×10^3	3.8×10^3	0.42	81.8
18	2.4×10^{-6}	4.7×10^3	6.2×10^3	3.8×10^3	0.39	78.4
19	3.9×10^{-6}	7.1×10^3	1.4×10^4	3.8×10^3	0.53	62.2
20	3.8×10^{-6}	7.2×10^3	1.3×10^4	3.7×10^3	0.52	62.2
21	2.6×10^{-6}	3.6×10^3	6.8×10^3	5.6×10^3	0.39	82.0
22	2.7×10^{-6}	4.6×10^3	6.6×10^3	5.6×10^3	0.36	78.9
23	4.2×10^{-6}	6.3×10^3	1.5×10^4	5.6×10^3	0.52	64.4
24	4.2×10^{-6}	6.7×10^3	1.4×10^4	5.5×10^3	0.51	64.1
25	3.5×10^{-6}	7.9×10^3	1.2×10^4	2.7×10^3	0.49	60.3
26	2.5×10^{-6}	5.0×10^3	7.5×10^3	2.7×10^3	0.45	73.2
27	3.1×10^{-6}	5.4×10^3	1.0×10^4	3.8×10^3	0.50	68.9
28	2.4×10^{-6}	4.3×10^3	6.4×10^3	3.8×10^3	0.40	79.5
29	3.0×10^{-6}	4.6×10^3	9.7×10^3	5.6×10^3	0.45	73.6
30	2.4×10^{-6}	3.8×10^3	5.5×10^3	5.6×10^3	0.33	84.6

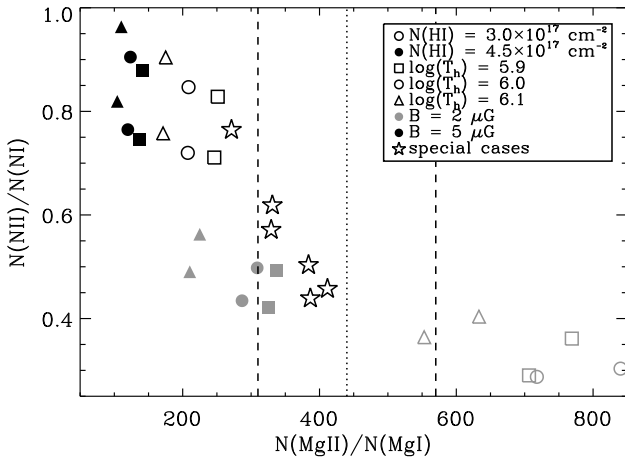


Fig. 4. Model results for $N(\text{N II})/N(\text{N I})$ versus $\text{Mg II}/\text{Mg I}$. The symbols have the same meaning as in Figure 3. In this case the models with higher $n(\text{H}^0)$ lie below and slightly to the left of those with lower density. $N(\text{N II})/N(\text{N I})$ is an indicator of cloud ionization fraction while $\text{Mg II}/\text{Mg I}$ goes as $1/n_e$. The dotted line is the observed value for $\text{Mg II}/\text{Mg I}$ and the dashed lines indicate the $1 - \sigma$ error range for the value. We see that models that match the observed ratio all correspond to relatively low ionization, $X(\text{H}) \sim 0.20 - 0.27$ in the CHM.

out evaporation that is consistent with the data we find $n(\text{H}^0) = 0.186 \text{ cm}^{-3}$, $n_e = 0.052 \text{ cm}^{-3}$. Including the PUI Ne data as

a constraint narrows the density results to $n(\text{H}^0) \approx 0.19 \text{ cm}^{-3}$ and $n_e = 0.06 - 0.07 \text{ cm}^{-3}$. For these densities to stray out of this range would appear to require significant errors in the underlying comparison data, e.g. $n(\text{He}^0)$ in the CHM, or substantial non-equilibrium ionization effects in the LIC. The variation in the interstellar radiation field between the different models that match the data give us some degree of confidence that these densities are not highly sensitive to the details of the radiation field. These results require that the H filtration factor is ~ 0.47 , well within the range of calculated values (see next section and Table 1). Note that the range $n_e = 0.05 - 0.08 \text{ cm}^{-3}$ corresponds to an electron plasma frequency of 2.0–2.5 kHz, which is the frequency of the mysterious weak radio emission detected beyond the termination shock in the outer heliosphere (Gurnett & Kurth 2005; Mitchell et al. 2004).

5.2. Hydrogen Filtration Factor

Tracers of H^0 inside of the termination shock, after filtration, include the $\text{H I Ly}\alpha$ backscattered radiation, H pickup ions, and the slowdown of the solar wind at distances beyond 5 AU from mass-loading by H PUIs. Models of the $\text{Ly}\alpha$ glow observed by the Voyager 1 and 2 at 39 AU and 32 AU upwind, and Pioneer 10 at 23 AU downwind, determine a LIC density of $n(\text{H}^0) \sim 0.18 - 0.19 \text{ cm}^{-3}$, with electron densities of $n_e \sim 0.05 - 0.06 \text{ cm}^{-3}$ (Gangopadhyay et al. 2006). Observations of H PUI ions indicate that $n(\text{H}^0) = 0.103 \pm 0.010 \text{ cm}^{-3}$, inside of the termination shock (Gloeckler & Fisk 2007). The observed slow-down of the solar wind speed as a function of heliocentric distance, due to mass-loading of the solar wind by interstellar pickup ions,

Table 7. Elemental Gas Phase Abundances (ppm)

Model No.	Element						
	C	N	O	Mg	Si	S	Fe
14	589	40.7	295	5.89	7.24	14.1	2.24
25	631	66.1	437	7.76	10.0	19.5	3.09
26	661	46.8	331	6.61	8.13	15.8	2.51
27	759	64.6	437	8.71	10.7	20.9	3.31
28	708	45.7	331	7.08	8.32	16.6	2.57
29	813	64.6	437	9.33	11.0	21.9	3.39
30	741	46.8	331	7.41	8.51	17.0	2.63
42	724	39.8	295	6.76	7.76	15.1	2.34

indicates that $n(\text{H}^0) \sim 0.09 \text{ km s}^{-1}$ at the termination shock (Richardson et al. 2006). These data, combined with our results, restrict the H filtration factor to the range $f = 0.45 - 0.59$, with $f \sim 0.53$ providing excellent agreement with both data and models (Mueller et al. 2007; Müller & Zank 2004; Gloeckler & Fisk 2007).

5.3. Gas-Phase Abundances

The LIC photoionization models are forced to match the observed set of column densities and $n(\text{He}^0)$ inside of the heliosphere (Table 1, 3). The gas-phase abundances of most elements are treated as free parameters that can be varied in order to match observed column densities, so that the successful models yield elemental abundances for the LIC that are automatically corrected for unobserved H^+ (Table 7). The exceptions are that He, Ne, and Ar abundances are assumed to be 10^5 ppm, 123 ppm and 2.82 ppm, respectively. In the models, $N(\text{C II}^*)$ is a constraint on both the C abundance (in place of the heavily saturated C II 1335Å line) and n_e , such that the product of the abundance and n_e is more tightly limited than either quantity individually. The requirement to match both $N(\text{C II}^*)$ and $n(\text{He}^0)$ effectively restricts the ionization fraction of H, which in turn limits O and N ionization whose ionizations are tied by charge transfer to the H ionization at LIC temperatures.

Early studies showed that the abundances of refractory elements in the very local ISM are enhanced compared to abundances in cold disk gas (Marschall & Hobbs 1972; Stokes 1978; Frisch 1981). Throughout warm and cold disk gas, the underabundances of refractory elements compared to solar abundances (by factors of $10^{-1} - 10^{-4}$) are taken to represent depletion onto interstellar dust grains (e.g. Savage & Sembach 1996). This view is supported by the correlation found between elemental depletions and the temperature characteristic of condensation at solar pressure and composition (Ebel 2000), and requires that there be a reference abundance pattern that characterizes the cloud, and remains constant over the cloud lifetime as atoms are exchanged between the gas and dust phases. Below (§5.4) we compare solar abundances with observed gas-phase abundances to predict the gas-to-dust mass ratios for the LIC, based on the assumption that LIC gas and dust have remained coupled over the cloud lifetime.

An important question is whether the LIC and the CHM have solar abundances. Isotopes of ^{18}O and ^{22}Ne isotopes measured in the ACR population suggest that this is so. ACRs are characterized by a rising particle flux for energies below 10–50 MeV/nucleon, and this characteristic spectral signature is seen for ^{16}O , ^{18}O , ^{20}Ne , and ^{22}Ne . Ratios of $^{16}\text{O}/^{18}\text{O} \sim 500$ and $^{20}\text{Ne}/^{22}\text{Ne} \sim 13.7$ are found for both the ACRs and solar ma-

Table 8. Solar Abundances (ppm)

	Grevesse Sauval (1998)	Holweger (2001)	Lodders (2003)	Asplund et al. (2005)
C	334 ± 46	391(+110, -86)	290 ± 27	247 ± 28
N	84 ± 12	85.3 ⁺²⁵ ₋₁₉	82 ± 20	61 ± 8
O	683 ± 94	545 ⁺¹⁰⁷ ₋₉₀	579 ± 66	460 ± 53
Ne	121 ± 17	100 ⁺¹⁷ ₋₁₅	91 ± 21	70 ± 10
Mg	38 ± 4	34.5 ^{+5.1} _{-4.5}	41 ± 2	33 ± 7
Si	35 ± 4	34.4 ^{+4.1} _{-3.7}	41 ± 2	32 ± 3
S	22 ± 5	-	18 ± 2	14 ± 2
Ar	2.54 ± 0.35	-	4.24 ± 0.77	1.54 ± 0.28
Fe	32 ± 4	28.1 ^{+5.8} _{-4.8}	35 ± 2	28 ± 3

terial, indicating that the CHM and solar material have similar compositions (Leske et al. 2000; Leske 2000). We therefore adopt solar abundances as the underlying reference abundance pattern for the LIC.

Unfortunately, considerable uncertainty exists in the solar abundances of volatile elements such as O and S, which have low condensation temperatures (T_{cond} , 180 K and 700 K respectively). Solar abundances are determined from photospheric data (C, N, O, Mg, Si, S, Fe), the solar wind (Ar, Ne), solar active regions (Ne), and helioseismic data (He); abundances of non-volatile elements are also found from meteoritic data (Grevesse & Sauval 1998; Holweger 2001; Lodders 2003; Asplund et al. 2005). Solar abundances for volatile elements found from recent three-dimensional hydrodynamic photospheric models (e.g. Holweger 2001, Asplund et al. 2005) are not in agreement with the earlier values. Solar abundances from these studies are listed in Table 8. Our results, discussed below, indicate that if the LIC has a solar abundance composition, as indicated by the ^{18}O and ^{22}Ne data, then the lower abundances found by Asplund et al. are preferred by our models.

Ne: In these models we have assumed the Ne abundance is 123 ppm (Anders & Grevesse 1989), but estimates of the solar Ne abundance range down to 78 ppm (Asplund et al. 2005, after adding 0.05 dex to account for gravitational settling of the elements, Grevasse, private communication). The predicted densities of $n(\text{Ne I})$ in the CHM for models 26 and 28 (Table 4) are in agreement with the most recent PUI results for Ne (Table 1), and neon densities as low as $\text{Ne}/\text{H} \sim 100$ are allowed when filtration is included. The CHM Ne abundances indicated by these results appear to be consistent with Ne abundances and ionization levels in the global ISM. The Ne abundance in the Orion nebula is 100 ppm (Simpson et al. 2004). Takei et al. (2002) measured X-ray absorption edges formed by Ne and O in the interstellar gas and dust towards Cyg X-2, and found abundances of $\text{Ne}/\text{H} \sim 92$ ppm and $\text{O}/\text{H} \sim 579$ ppm when both atomic and compound forms in the sightline were included. Juett et al. (2006) observed the X-ray absorption edges of Ne and O towards nine X-ray binaries which sampled both neutral and ionized warm material, and found that the ionized states formed in the ionized material have the ratio $\text{Ne III}/\text{Ne II} \sim 0.23$. This value is identical to the predictions of model 26, $\text{Ne III}/\text{Ne II} \sim 0.23$, a fortuitous agreement that may indicate that the EUV radiation field in the CHM is similar to the generic galactic EUV field in the solar vicinity.

Ar: Solar Ar abundance determinations range between $\text{Ar}/\text{H} = 1.51 - 4.17$ ppm (Table 8); we have assumed $\text{Ar}/\text{H} = 2.82$ ppm. The predicted Ar density at the Sun is within the uncertainties of the PUI data, although the range of possible filtration factors (0.64 – 0.95, see §2.2) allow considerable leeway.

O: In the warm ISM such as the LIC, the ionizations of oxygen and hydrogen are tightly coupled over timescales of ~ 100 years due to charge transfer (Field & Steigman 1971), so that the assumed $N(\text{H I})$ combined with $N(\text{O I})$ measurements are a *de facto* constraint on the O abundance in the gas. The two best models (26, 28) correspond to $\text{O}/\text{H} = 331$ ppm, however the O column density measurements are based on the saturated 1302\AA line, and have $\sim 35\%$ uncertainty. The PUI measurements of O/H in the CHM, $\text{O}/\text{H} = 178 - 427$ when filtration uncertainties are included (Table 1), are consistent with the ϵ CMa LIC data. If O filtration is comparable to H filtration, ~ 0.66 , then $\text{O}/\text{H} = 342 - 426$. The solar O abundance is in the range 407–689 ppm (inclusive of uncertainties, Table 8). Based on the PUI data alone, O may be present in the gas-phase with solar abundances, with the overlap indicating solar abundances of $\text{O}/\text{H} = 407 - 427$ ppm as found by Asplund et al. However if the modeled LIC value of $\text{O}/\text{H} \sim 331$ is accurate, then it appears that there must be some depletion of O in the LIC.

The ratio $N(\text{O I})/N(\text{H I})$ is measured in both low and high extinction clouds. Oliveira et al. (2003) used unsaturated O I lines in the $910\text{--}1100\text{\AA}$ interval and found $\text{O I}/\text{H I} = 317 \pm 19$ ppm for ~ 30 sightlines that included both types of material. Sightlines with detected H_2 , $N(\text{H}) > 10^{20.5} \text{ cm}^{-2}$ and $\langle n_{\text{H}} \rangle = 0.1 - 3.3$, yield $\text{O}/\text{H} = 319 \pm 14$ ppm (Meyer et al. 1997). A survey of 19 stars with an average distance of 2.6 kpc by (André et al. 2003) found $\text{O I}/\text{H I} = 408 \pm 14$ ppm, where the long sightline and high average value $N(\text{H})/E(B-V) = 6.3 \times 10^{21} \text{ cm}^{-2} \text{ mag}^{-1}$ indicate a bias towards sightlines containing many clouds that individually have low extinctions. A larger sample of 56 sightlines for a range of extinctions and distances show that sightlines with higher average mean densities, $\langle n_{\text{H}} \rangle$, show $\text{O}/\text{H} = 284 \pm 12$ ppm, versus $\text{O}/\text{H} = 390 \pm 10$ ppm for stars with low values of $\langle n_{\text{H}} \rangle$ (Cartledge et al. 2004). For comparison, solar abundance studies yield a range of $\sim 410\text{--}780$ ppm (when uncertainties are included, Table 8).

C: The best Models 26 and 28 yield a gas-phase abundance of C of $\text{C}/\text{H} = 661$ and 708 compared to solar abundances of 220–500 (including uncertainties, Table 8). This is consistent with our earlier results (Slavin & Frisch 2006) indicating that C is overabundant in the LIC. We believe that shock destruction of carbonaceous grains, perhaps combined with some local spatial decoupling between carbonaceous and silicate grains, may explain these findings. Singly-ionized carbon is an important coolant in the LIC (§5.5), so this C overabundance is also required to maintain the temperature of the CHM at the observed value. The carbon abundance obtained here indirectly depends on the $\text{Mg II} \rightarrow \text{Mg I}$ dielectronic recombination coefficient that determines the ratio $\text{Mg II}/\text{Mg I}$, since that ratio is used as a criteria for the best models. It is promising that the same ionization correction that gives the C abundance also successfully predicts Ne ionization in global WPIM and the S abundances in the LIC. In contrast, sightlines with cold ISM show C abundances of $\text{C}/\text{H} = 141$ ppm (Sembach et al. 2000) and 135 ± 46 ppm (Sofia et al. 1997).

N: The best models (26 and 28) find $\text{N}/\text{H} = 46\text{--}47$ ppm, compared to solar values of 53–110 ppm (when uncertainties are included). These results are consistent with the PUI results, $\text{N}/\text{H} \sim 19 - 47$ ppm, after filtration factor uncertainties are included.

S: The best models predict $\text{S}/\text{H} = 16\text{--}17$, compared to solar values of 12–27 (including uncertainties, see Table 8). Sulfur is generally expected to have little or no depletion onto dust grains in the diffuse ISM.

Mg, Si, Fe: These refractory elements are observed in the LIC gas with abundances far below solar (factors of 3–15). Approximately 99%, 82%, and 76% of the Fe, Mg, and Si, re-

spectively, are depleted onto interstellar dust grains, where they have the approximate ratios of 26–30:26–31:24–27, respectively (or, to within uncertainties, $\sim 1:1:1$). These elements all have FIP < 13.6 eV and are therefore at least once ionized in the LIC. Both Fe and Si are almost entirely singly ionized, while Mg has a significant ion fraction that is twice ionized (for example, $\sim 15\%$ in model 26). These refractory abundances thus remain highly subsolar, even after ionization corrections are made, indicating that these elements are substantially depleted onto interstellar dust grains. In contrast to C, however, the silicate dust in the LIC that carries the missing Mg, Si, and Fe has experienced far less destruction than the carbonaceous grains. This result is consistent with theoretical models of grain destruction that predict that the interstellar grain size distribution will be skewed towards large dust grains, composed of silicates, inside of superbubble cavities consisting of hot low density ISM that has been shocked, while tiny carbonaceous grains are more likely to be destroyed by thermal sputtering in the hot gas of supernova remnants (Jones et al. 1996; Slavin et al. 2004).

Ca II, Na I: Weak lines of the trace ionization species Ca II and Na I are common diagnostics of ionization and abundance for interstellar clouds, including the partially ionized LIC; Na I is also frequently used as a diagnostic of the H column density. We note that our models show that the ratios $N(\text{Ca II})/N(\text{Na I})$, $N(\text{Na I})/N(\text{H})$, and $N(\text{Na I})/N(\text{H I})$ vary by 30%, 77%, and 93%, respectively, between the best models (Models 26–30, 42). As trace ionization species, the densities of Na I and Ca II are highly sensitive to volume density, $n(\text{Na I}), n(\text{Ca II}) \propto n_{\text{H}} n_e$. We therefore conclude that Na I and Ca II are imprecise diagnostics of ionization levels, H density, and abundances in warm partially ionized clouds.

5.4. Gas-to-Dust Mass Ratio

Because the abundances are automatically corrected for unobserved H^+ , we use the model results to infer the total mass of the interstellar dust, providing that the gas and dust in the LIC form a coupled and closed system that evolves together as the cloud moves through the LSR. The LIC LSR velocity is 16–21 pc/Myr, so that a LIC origin related to the Loop I or Scorpius–Centaurus superbubble would require that the LIC gas and dust remained a closed system over timescales of 4–5 Myr (Frisch & Slavin 2006; Frisch 1981). Gas-to-dust mass ratios calculated from the best models (26 and 28) using the missing-mass argument⁴ are in the range $R_{\text{G/D}} = 152 - 285$, depending on solar abundances. The detailed information about $R_{\text{G/D}}$ for different assumptions and the different models is listed in table 9.

For comparison, $R_{\text{G/D}}$ determined from comparisons of *in situ* observations of interstellar dust inside of the solar system, compared to the gas densities of these models, yield $R_{\text{G/D}} = 116\text{--}127$ (Table 9 Landgraf et al. 2000; Altobelli et al. 2004). The *in situ* $R_{\text{G/D}}$ is an upper limit, since the smallest interstellar dust grains (radii $0.1\mu\text{m}$) are excluded from the heliosphere by Lorentz coupling to the interstellar magnetic field which is draped over the heliosphere.

In all cases, $R_{\text{G/D}}$ determined from comparing *in situ* dust measurements with the CHM gas mass determined by each model suggests that the interstellar dust flowing into the heliosphere is concentrated in the ISM close to the Sun, compared to the overall LIC sightline towards ϵ CMa. The lower solar abun-

⁴ This argument assumes that the ISM reference abundances, in this case solar abundances, represent the sum of the atoms in the gas plus the dust (Frisch et al. 1999).

Table 9. Gas-to-Dust Mass Ratios from Models and In Situ Observations

Source	Model						
	14	26	27	28	29	30	42
GS98	139.9	151.6	200.2	152.0	201.4	152.8	140.8
Lodders	161.5	177.2	243.8	177.8	244.9	178.8	162.6
Asplund	248.7	284.7	483.4	285.0	487.8	286.8	249.9
In Situ ^a	116.0	116.8	124.3	116.5	126.5	117.0	108.4

^a The in situ dust flux is from Landgraf et al. (2000), corrected downwards by 20% as recommended by Altobelli et al. (2004) to correct for side-wall impacts.

Table 10. Major Heat Sources in LIC Gas^a

Source ^b	Fraction of Heating
H I	0.657
He I	0.248
dust	0.055
He II	0.016
cosmic rays	0.010

^a Results for model 26. Other models are qualitatively the same, though there are some quantitative variations.

^b For lines with ion names, the source here denotes the ion that is photoionized. Dust heating comes from photoelectric ejection by photons of the background FUV radiation field. Cosmic ray heating comes from electron impact ionization of the gas and direct heating of the electrons in the LIC plasma by the cosmic ray electrons.

dances of Asplund et al. leave fewer volatile elements that are required to be trapped in the dust, and produces stronger disagreements with $R_{G/D}$ determined from in situ data. We do not understand this result, which we have found previously (Frisch et al. 1999). Since $R_{G/D}$ responds to the mass of Fe in the dust grain (Frisch & Slavin 2003), we surmise this difference indicates inhomogeneous mixing of the gas and silicate dust over the ~ 0.63 pc extent of the LIC.

5.5. Heating and Cooling Rates

The heating and cooling rates for Model 26 are listed in Tables 10 and 11. The primary heat sources are photoelectrons from the ionization of H⁰ and He⁰, with dust and cosmic ray heating contributing less than 7% of the heating. The dominant source of cooling is the [C II] 157.6 μm fine-structure line, making up 43% of the total. This is more than twice the contribution of any other coolant. Nearly all the cooling is due to optical and IR forbidden lines with many lines contributing at the $\sim 1\%$ level. H recombination, free-free emission and dust, through the capture of electrons onto grain surfaces, also contribute at about a 2% level. The importance of C II as both a constraint on the C abundance in our models as well as a major coolant means that any model that aims to reduce the abundance of C to a solar level faces severe difficulties. The models with LIC temperatures in the $T_{\text{He}^0} = 6300 \pm 340$ K range indicated by the *in situ* He⁰ data all require supersolar abundances of C. The total heating/cooling rate for the LIC at the Sun for this model is 3.55×10^{-26} ergs cm^{-3} s^{-1} .

Table 11. Major Coolants in LIC Gas^a

Ion/Line	Fraction of Cooling
[C II] 157.6 μm	0.428
[S II] 6731 \AA	0.145
Fe II (total)	0.074
[Si II] 34.8 μm	0.065
[Ne II] 12.8 μm	0.035
[O I] 63.2 μm	0.028
H recomb.	0.024
dust	0.024
[Ne III] 15.6 μm	0.020
[N II] 6584 \AA	0.018
net free-free	0.018
[O I] 6300 \AA	0.017
[O II] 3727 \AA	0.011
[Ar II] 6.98 μm	0.011

^a Results for model 26. Other models show similar results.

5.6. Radiation Field

Recently it has been proposed that a significant portion of the SXRb can be attributed to charge transfer between the solar wind ions (e.g., O 7 and O 8) and interstellar neutrals (Cravens 2000; Smith et al. 2005; Snowden et al. 2004). While it seems at present that some fraction of the low energy X-rays are from this mechanism, it is unclear how large that fraction is. We note that basing the properties of the local hot plasma in the galactic plane on SXRb emission at energies $E > 0.3$ keV is problematical. Kashyap et al. (1992) have shown that the contribution of main-sequence stars to the SXRb at $E < 0.3$ keV is minor ($< 3\%$), but it rises to 7 – 40% for $\sim 0.4 - 0.9$ keV. (Bellm & Vaillancourt 2005) have compared the Wisconsin B and Be band data with the ROSAT R12 data, and concluded that the observed anticorrelation between R12 and $N(\text{H I})$ indicates that more than 34% of the SXRb generated in the Galactic disk must come from the Local Bubble. They also concluded that a heavily depleted plasma with $\log T \sim 5.8$ is consistent both with the McCammon et al. (2002); Sanders et al. (2001) X-ray spectral data, and the upper limits set on the EUV emission by CHIPS (Hurwitz et al. 2004). When the Robertson & Cravens (2003) models of SXRb production by charge-exchange with the solar wind are considered, then only half of the SXRb in the plane is required to arise from a hot local plasma. We also note that the atomic physics for the calculation of the low energy part of the emission is still quite uncertain (V. Kharchenko, private communication). At this point we take the simple approach of ignoring the charge transfer emission, though we plan to consider its possible impact in future work.

5.7. LIC Pressure

The strength of the interstellar magnetic field in the LIC is unknown. The best models (26 and 28) have a thermal pressure of $\sim 2300 \text{ cm}^{-3}$ K for the LIC. If the thermal and magnetic pressures are equal, this indicates that the magnetic field strength is $B = 2.8 \mu\text{G}$, which is consistent with the field strengths adopted for these models. (Recall these field strengths were used because they produced good agreement of the photoionization models with the observed values of He I density and temperature.) We note that if the cosmic ray and thermal gas pressures are comparable, then the static pressure of the LIC is $\sim 5700 \text{ cm}^{-3}$ K.

6. Conclusions

There are many uncertainties regarding the detailed properties of the ionizing interstellar radiation field incident on the LIC. The wealth of data we have on the LIC, both from absorption line studies and *in situ* measurements by spacecraft in the heliosphere, provide us with strong constraints on the ionization and composition of the LIC and particularly the CHM. By exploring a range of models for the ISRF we find that while a fairly broad range of radiation fields can produce photoionization consistent with the data, other outputs from the models fall within a relatively narrow range of values. Our results for the models explored in this paper in which we require our models to be consistent with the LIC component of the absorption lines observed towards ϵ CMa include:

1. For a range of assumptions regarding the H I column density of the LIC, $N(\text{H I}) = (3.0 - 4.5) \times 10^{17} \text{ cm}^{-2}$, and temperature of the hot gas of the Local Bubble, $\log T_h = 5.9, 6.0$ and 6.1 , we are able to find model parameters that allow a match of the model results with best observed quantities, $n(\text{He}^0)$, $T(\text{He}^0)$ and $N(\text{Mg II})/N(\text{Mg I})$. For these models we assume that the cloud is evaporating because of thermal conduction between the hot Local Bubble gas and the warm LIC gas and include the emission from the cloud boundary.
2. For the best models in terms of fits to data, the required input parameters are: initial (i.e. at the outer edge of the cloud) total H density, $n(\text{H}) \approx 0.21 - 0.23 \text{ cm}^{-3}$; and cloud magnetic field, $B_0 \leq 3.8 \mu\text{G}$.
3. If we assume that the magnetic field configuration reduces thermal conductivity at the boundary enough to prevent evaporation and ignore any radiation from the cloud boundary, we find that for most cases the radiation field does not cause sufficient heating to maintain the LIC at the temperature observed, $T = 6,300 \pm 340 \text{ K}$. One set of parameter choices, though, yields successful models. These parameters are $N(\text{H I}) = 4.5 \times 10^{17} \text{ cm}^{-2}$ and $\log T_h = 6.1$.
4. Despite the wide range of possible input parameters, the output values for quantities important for shaping the heliosphere are confined to a fairly small range: $n(\text{H}^0) = 0.19 - 0.20 \text{ cm}^{-3}$, and $n_e = 0.05 - 0.08 \text{ cm}^{-3}$.
5. Observations of PUIs, the H I Ly α glow, and the solar wind slow-down in the outer heliosphere, all yield a value of $n(\text{H}^0) \sim 0.1$ after filtration. Agreement with our results for the LIC is achieved for a H filtration factor of $f_H = 0.53^{+0.06}_{-0.07}$, in good agreement with theoretical filtration models.
6. Elements with ionization potentials 13.6–25 eV, e.g. H, He, N, O, Ne, and Ar, are partially ionized with fractional ionizations of $\sim 0.2 - 0.7$.
7. By requiring that the models match the column densities derived from absorption line data we are able to determine the necessary elemental abundances for several elements. We find that the abundances of N and O may be somewhat sub-solar, although if only the PUI data are considered O abundances appear solar. Sulfur is roughly solar, and C is substantially super-solar. Mg, Si and Fe are all sub-solar by factors of 3–15. We conclude that any carbonaceous dust in the LIC must have destroyed, while silicate dust has persisted. Except for the gas-to-dust mass ratio, these results are in better agreement with the lower solar abundances of Asplund et al. (2005).
8. The gas-to-dust mass ratio derived from missing mass in the gas-phase for our best models depends strongly on the assumed reference abundance set and range from 140–490. For these same models $R_{G/D} = 116 - 124$ based on the observed

flux of dust into the heliosphere. The discrepancy of these values is minimized, in fact leading to consistency within the errors, if one assumes an abundance set such as that of GS98 which has large abundances of the metals. The GS98 abundances lead to substantial O depletion, however, which is not easily explained.

9. These models also show that $N(\text{Ca II})/N(\text{Na I})$, $N(\text{Na I})/N(\text{H I})$, and $N(\text{Na I})/N(\text{H})$ all vary significantly between the best models because of the sensitivity of these trace ionization species to density and ionization.

Acknowledgements. We would like to thank George Gloeckler for sharing data with us prior to publication, and Alan Cummings for pointing out that the ACR isotopic data indicate that the LIC abundances are solar. We also thank the International Space Science Institute in Bern, Switzerland for hosting the “Determination of the Physical Hydrogen Parameters of the LIC from within the Heliosphere.” This research was supported by NASA Solar and Heliospheric Program grants NNG05GD36G and NNG06GE33G to the University of Chicago, and by the NASA grant NNG05EC85C to SWRI.

References

- Adams, T. F. & Frisch, P. C. 1977, *ApJ*, 212, 300
 Ajello, J. M. 1978, *ApJ*, 222, 1068
 Altobelli, N., Krüger, H., Moissl, R., Landgraf, M., & Grün, E. 2004, *Planet. Space Sci.*, 52, 1287
 Altun, Z., Yumak, A., Badnell, N. R., Loch, S. D., & Pindzola, M. S. 2006, *A&A*, 447, 1165
 Anders, E. & Grevesse, N. 1989, *Geochim. Cosmochim. Acta*, 53, 197
 André, M. K., Oliveira, C. M., Howk, J. C., et al. 2003, *ApJ*, 591, 1000
 Asplund, M., Grevesse, N., & Sauval, A. J. 2005, in *ASP Conf. Ser. 336: Cosmic Abundances as Records of Stellar Evolution and Nucleosynthesis*, 25–+
 Bellm, E. C. & Vaillancourt, J. E. 2005, *ApJ*, 622, 959
 Bertaux, J. L. & Blamont, J. E. 1971, *A&A*, 11, 200
 Bloch, J. J., Jahoda, K., Juda, M., et al. 1986, *ApJ*, 308, L59
 Bzowski, M. 2003, *A&A*, 408, 1155
 Cartledge, S. I. B., Lauroesch, J. T., Meyer, D. M., & Sofia, U. J. 2004, *ApJ*, 613, 1037
 Cheng, K. & Bruhweiler, F. C. 1990, *ApJ*, 364, 573
 Cowie, L. L. & McKee, C. F. 1977, *ApJ*, 211, 135
 Cravens, T. E. 2000, *ApJ*, 532, L153
 Cummings, A. C., Stone, E. C., & Steenberg, C. D. 2002, *ApJ*, 578, 194
 Dupuis, J., Vennes, S., Bowyer, S., Pradhan, A. K., & Thejll, P. 1995, *ApJ*, 455, 574
 Ebel, D. S. 2000, *J. Geophys. Res.*, 105, 10363
 Egger, R. J. & Aschenbach, B. 1995, *A&A*, 294, L25
 Ferland, G. J., Korista, K. T., Verner, D. A., et al. 1998, *PASP*, 110, 761
 Field, G. B. & Steigman, G. 1971, *ApJ*, 166, 59
 Frisch, P. & York, D. G. 1986, in *The Galaxy and the Solar System* (University of Arizona Press), 83–100
 Frisch, P. C. 1981, *Nature*, 293, 377
 Frisch, P. C. 2007, “Composition of Matter”, *Space Sciences Series of ISSI*, publ. Springer, 27, 00
 Frisch, P. C., Dorschner, J. M., Geiss, J., et al. 1999, *ApJ*, 525, 492
 Frisch, P. C., Grodnicki, L., & Welty, D. E. 2002, *ApJ*, 574, 834
 Frisch, P. C. & Slavin, J. D. 2003, *ApJ*, 594, 844
 Frisch, P. C. & Slavin, J. D. 2005, *Advances in Space Research*, 35, 2048
 Frisch, P. C. & Slavin, J. D. 2006, *Short Term Variations in the Galactic Environment of the Sun, in it Solar Journey: The Significance of Our Galactic Environment for the Heliosphere and Earth*, Ed. P. Frisch (Springer), 133–193
 Gangopadhyay, P., Izmodenov, V. V., Gruntman, M., & Judge, D. L. 2006, *ApJ*, 637, 786
 Gloeckler, G. & Fisk, L. 2007, “Composition of Matter”, *Space Sciences Series of ISSI*, publ. Springer, 27, 00
 Gloeckler, G. & Geiss, J. 2004, *Advances in Space Research*, 34, 53
 Gloeckler, G. & Geiss, J. 2007, *A&A*, this volume
 Gondhalekar, P. M., Phillips, A. P., & Wilson, R. 1980, *A&A*, 85, 272
 Grevesse, N. & Sauval, A. J. 1998, *Space Science Reviews*, 85, 161
 Gry, C. & Jenkins, E. B. 2001, *A&A*, 367, 617
 Gurnett, D. A. & Kurth, W. S. 2005, *Science*, 309, 2025
 Hébrard, G., Mallouris, C., Ferlet, R., et al. 1999, *A&A*, 350, 643
 Henry, R. C. 2002, *ApJ*, 570, 697
 Holweber, H. 2001, in *AIP Conf. Proc. 598: Joint SOHO/ACE workshop “Solar and Galactic Composition”*, 23–+
 Hurwitz, M., Sasseen, T. P., & Sirk, M. M. 2004, *ArXiv Astrophysics e-prints*

- Izmodenov, V., Malama, Y., Gloeckler, G., & Geiss, J. 2004, *A&A*, 414, L29
- Jones, A. P., Tielens, A. G. G. M., & Hollenbach, D. J. 1996, *ApJ*, 469, 740
- Juett, A. M., Schulz, N. S., Chakrabarty, D., & Gorczyca, T. W. 2006, *ApJ*, 648, 1066
- Kashyap, V., Rosner, R., Micela, G., et al. 1992, *ApJ*, 391, 667
- Lallement, R., Bertin, P., Ferlet, R., Vidal-Madjar, A., & Bertaux, J. L. 1994, *A&A*, 286, 898
- Lallement, R., Vidal-Madjar, A., & Ferlet, R. 1986, *A&A*, 168, 225
- Landgraf, M., Baggaley, W. J., Grün, E., Krüger, H., & Linkert, G. 2000, *J. Geophys. Res.*, 105, 10343
- Landsman, W. B., Henry, R. C., Moos, H. W., & Linsky, J. L. 1984, *ApJ*, 285, 801
- Lehner, N., Jenkins, E., Gry, C., et al. 2003, *ApJ*, 595, 858
- Leske, R. A. 2000, in *AIP Conf. Proc. 516: 26th International Cosmic Ray Conference*, ICRC XXVI, ed. B. L. Dingus, D. B. Kieda, & M. H. Salamon, 274–+
- Leske, R. A., Mewaldt, R. A., Christian, E. R., et al. 2000, in *AIP Conf. Proc. 528: Acceleration and Transport of Energetic Particles Observed in the Heliosphere*, ed. R. A. Mewaldt, J. R. Jokipii, M. A. Lee, E. Möbius, & T. H. Zurbuchen, 293–+
- Linsky, J. L. & Wood, B. E. 1996, *ApJ*, 463, 254
- Lodders, K. 2003, *ApJ*, 591, 1220
- Möbius, E., Bzowski, M., Chalov, S., et al. 2004, *A&A*, 426, 897
- Müller, H.-R. & Zank, G. P. 2004, *Journal of Geophysical Research (Space Physics)*, 7104
- Marschall, L. A. & Hobbs, L. M. 1972, *ApJ*, 173, 43
- McCammon, D., Almy, R., Apodaca, E., et al. 2002, *ApJ*, 576, 188
- McCammon, D., Burrows, D. N., Sanders, W. T., & Kraushaar, W. L. 1983, *ApJ*, 269, 107
- McClintock, W., Henry, R. C., Linsky, J. L., & Moos, H. W. 1978, *ApJ*, 225, 465
- McClintock, W., Linsky, J. L., Henry, R. C., & Moos, H. W. 1975, *ApJ*, 202, 733
- Meyer, D. M., Cardelli, J. A., & Sofia, U. J. 1997, *ApJ*, 490, L103
- Mitchell, J. J., Cairns, I. H., & Robinson, P. A. 2004, *Journal of Geophysical Research (Space Physics)*, 109, 6108
- Mueller, H.-R., Florinski, V., Heerikhuisen, J., et al. 2007, *â*, submitted
- Oliveira, C. M., Hébrard, G., Howk, J. C., et al. 2003, *ApJ*, 587, 235
- Parravano, A., Hollenbach, D. J., & McKee, C. F. 2003, *ApJ*, 584, 797
- Quémerais, E., Lallement, R., Bertaux, J.-L., et al. 2006a, *A&A*, 455, 1135
- Quémerais, E., Lallement, R., Ferron, S., et al. 2006b, *Journal of Geophysical Research (Space Physics)*, 111, 9114
- Raymond, J. C. & Smith, B. W. 1977, *ApJS*, 35, 419
- Richardson, J. D., Wang, C., & Burlaga, L. F. 2004, *Advances in Space Research*, 34, 150
- Richardson, J. D., Wang, C., & Zhang, M. 2006, in *AIP Conf. Proc. 858: Physics of the Inner Heliosheath*, ed. J. Heerikhuisen, V. Florinski, G. P. Zank, & N. V. Pogorelov, 110–115
- Ripken, H. W. & Fahr, H. J. 1983, *A&A*, 122, 181
- Robertson, I. P. & Cravens, T. E. 2003, *Journal of Geophysical Research (Space Physics)*, 108, 6
- Rucinski, D., Cummings, A. C., Gloeckler, G., et al. 1996, *Space Science Reviews*, 78, 73
- Sanders, W. T., Edgar, R. J., Kraushaar, W. L., McCammon, D., & Morgenthaler, J. P. 2001, *ApJ*, 554, 694
- Savage, B. D. & Sembach, K. R. 1996, *ApJ*, 470, 893
- Sembach, K. R., Howk, J. C., Ryans, R. S. I., & Keenan, F. P. 2000, *ApJ*, 528, 310
- Simpson, J. P., Rubin, R. H., Colgan, S. W. J., Erickson, E. F., & Haas, M. R. 2004, *ApJ*, 611, 338
- Slavin, J. D. 1989, *ApJ*, 346, 718
- Slavin, J. D. & Frisch, P. C. 2002, *ApJ*, 565, 364
- Slavin, J. D. & Frisch, P. C. 2006, *ApJ*, 651, L37
- Slavin, J. D., Jones, A. P., & Tielens, A. G. G. M. 2004, *ApJ*, 614, 796
- Smith, R. K., Edgar, R. J., Plucinsky, P. P., et al. 2005, *ApJ*, 623, 225
- Snowden, S. L., Collier, M. R., & Kuntz, K. D. 2004, *ApJ*, 610, 1182
- Snowden, S. L., Cox, D. P., McCammon, D., & Sanders, W. T. 1990, *ApJ*, 354, 211
- Snowden, S. L., Egger, R., Finkbeiner, D. P., Freyberg, M. J., & Plucinsky, P. P. 1998, *ApJ*, 493, 715
- Snowden, S. L., Egger, R., Freyberg, M. J., et al. 1997, *ApJ*, 485, 125
- Snowden, S. L., McCammon, D., & Verter, F. 1993, *ApJ*, 409, L21
- Sofia, U. J., Cardelli, J. A., Guerin, K. P., & Meyer, D. M. 1997, *ApJ*, 482, L105
- Stokes, G. M. 1978, *ApJS*, 36, 115
- Takei, Y., Fujimoto, R., Mitsuda, K., & Onaka, T. 2002, *ApJ*, 581, 307
- Thomas, G. E. & Krassa, R. F. 1971, *A&A*, 11, 218
- Vallerga, J. 1996, *Space Sci. Rev.*, 78, 277
- Vallerga, J. 1998, *ApJ*, 497, 921
- Weller, C. S. & Meier, R. R. 1981, *ApJ*, 246, 386
- Witte, M. 2004, *A&A*, 426, 835
- Witte, M., Banaszekiewicz, M., & Rosenbauer, H. 1996, *Space Science Reviews*, 78, 289
- Wood, B. E., Linsky, J. L., & Zank, G. P. 2000a, *ApJ*, 537, 304
- Wood, B. E., Linsky, J. L., & Zank, G. P. 2000b, *ApJ*, 537, 304
- Wood, B. E., Redfield, S., Linsky, J. L., Müller, H.-R., & Zank, G. P. 2005, *ApJS*, 159, 118
- York, D. G. 1974, *ApJ*, 193, L127

List of Objects

‘ ϵ CMa’ on page 2

‘Sirius’ on page 2